Seismic velocity investigation of the Steen River impact structure, northern Alberta

Matteo Niccoli, Alan R. Hildebrand, and Don C. Lawton

ABSTRACT

A specialized seismic velocity survey was undertaken early in 2000 to better understand the structure of the ~25 km-diameter Steen River crater. A seismic refraction line was augmented by a coincident 3-C seismic line located across the crater's rim uplift. Autonomous 3-C Orion seismometers recorded these and several other reflection lines to explore velocity anisotropies. Editing and reduction of the Orion data were done with new programs developed in Perl and Matlab. In Matlab, the data were displayed as Orion receiver gathers, and shown to be very similar to standard reflection seismic data, as expected. Data were further processed in Promax to improve the continuity of the first breaks; the picked first breaks were exported to GLI3D where 2D depth and velocity models were created, aided by constraints from well logs. The velocity models for two lines intersecting at the crater's rim, one parallel to the rim, the other one orthogonal, are compared at the well tie, and display significant differences that are interpreted as a combination of structural and fracture induced anisotropy effects. The conclusions are supported by 3D refraction modelling of the same lines and by interval velocity modelling on the rim parallel line and a different orthogonal line in the same area.

INTRODUCTION

The buried ~25 km-diameter Steen River impact structure of Alberta is the remnant of the largest known crater in the Western Canadian Sedimentary Basin (WCSB). The structure is located in northwest Alberta, approximately 700 kilometres northwest of Edmonton (Figure 1), in Townships 120 to123, Ranges 20 to 23, West of the 5th Meridian. The crater lies a few kilometres northwest of the large northeast trending Precambrian lineament known as the Hay River Shear Zone (Winzer, 1972).

FIG. 1. Area location.

A stratigraphic column of the area is shown in Figure 2, representing the transition from the western margin of the Hay River platform (a cratonic platform) to the

continental shelf. An unconformity truncates the Palaeozoic sequence; crater relief was still in excess of 50 m when completely transgressed by a marine depositional environment, although the crater rim experienced approximately 500 m of erosion before its burial. Above the unconformity, a Lower Cretaceous shale formation, whose age is approximately constrained to ~100 My, buries the impact structure. After its erosion and burial during the Cretaceous, uplift occurred with most recent, significant erosion of cover rocks during the Pleistocene glaciation. The crater has no surface expression (Robertson, 1997), and is defined by information derived from seismic data, well logs, and information from potential fields studies (Hildebrand et al., 1998). Integration of these data reveal an irregular, faulted, crater perimeter with rim uplift of up to ~100 m above regional. The central structural uplift has a radius of ~3 km, based on well control and magnetic field anomalies, and is located off centre towards the east.

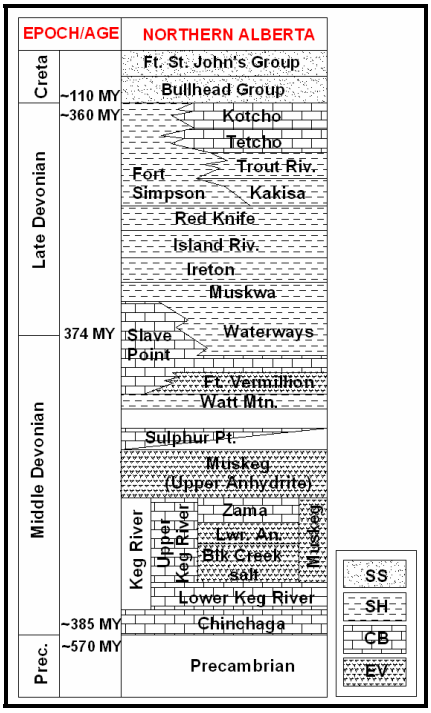

FIG. 2. Stratigraphic column of the Steen River area, after Fritz et al. (1991), and Hladiuck et al. (1999). SS=sandstone; SH=shale; CB=carbonate; EV=evaporite.

Robertson (1997), Hladiuk et al. (1999), and Hildebrand et al. (2000) provide background reviews of exploration and production activities at Steen River. During 2000 production was approximately 1,000 BOPD seasonally from the Keg River Formation and roughly 45 Mmcf/d gas from the Slave Point Formation. As of July 2002 production had decreased to ~500 BOPD as a maximum rate with some of the production still seasonal, and ~20 Mmcf/d gas in two gas plants and one pipeline transporting sour gas off site for processing.

The most common reservoir type formed by impacts is the crater rim uplift for both simple craters, such as Viewfield, a ~1.2 km diameter simple crater (e.g., Sawatsky, 1976) and complex craters, such as Steen River (Carrigy and Short 1968; Winzer 1972). As fracturing appears to dominate permeability at crater targets such as Steen River

(Hladiuk et al. 1999), characterization of this reservoir property is necessary to best exploit these impact-generated reservoirs. At Steen River, down-hole imaging done by Conoco Canada revealed fracturing in the reservoir rocks of the rim, and pressure data from production testing indicate a highly permeable reservoir with a dual porosity system (Hladiuk et al. 1999). The reservoir permeability and one component of the porosity are interpreted as largely reflecting rim fracturing. Characterizing this induced fracturing is also desirable in the context of considering impact structures as gas storage facilities. The zones of fracturing surrounding craters have long been known on a macro scale (e.g. Innes et al., 1964), and cratering literature contains numerous references to the zones of fracturing induced around craters. However, little quantitative determination of fracture occurrence, distribution, and orientation has been done.

Recently, P- and S-wave velocity anisotropies have been used to determine fracture abundances and orientation in several hydrocarbon-producing fields (e.g., Lynn et al. 1996; Bates et al. 1999; Gray et al. 1999; Tsvankin and Lynn 1999). On September 1999 we began a project funded by the COURSE program of the Alberta Department of Energy and Conoco Canada Resources Ltd to apply velocity methods in exploring the Steen River crater structure. We implemented a seismic refraction study tied to Conoco Canada's January 2000 seismic reflection program, which featured a half dozen crossing lines where seismic energy could be recorded both parallel (parallel lines) and perpendicular (radial lines) to the crater's rim (and at varying distances from the crater rim). The refraction survey gathered 3-C data using Orion seismometers loaned by the Geological Survey of Canada and David Eaton of The University of Western Ontario. Although the Conoco shoot was not a real 3D survey, so that not all azimuths and move outs were sampled, lines crossed nearly perpendicularly over the rim resulting in a geometry similar to that employed by Bates et al. (1999). We have generated depth and velocity models for two of these lines, and here compare the models at the well tie to study velocity anisotropies and thereby investigate the fracture systems associated with the crater's rim. We have also initiated a complementary seismic reflection study by modelling interval velocities for two lines intersecting over the crater's rim in the same area, and comparing the models at the well tie.

ORION SEISMOMETERS EXPERIMENT

Orion deployment

Orion self-contained seismometers were placed at the crossings of several seismic reflection lines during the commercial seismic shoot (Figure 3). The shot interval for the 1-kg charges along each of the lines was 60 m. In order to try to better understand the interior region of the crater, the eight Orion seismometers were deployed along the 22 km long refraction line R1 during the shooting of both it and the 3-C line. In addition to the 1-kg charges along the 3-C line, 10-kg charges were located every 300 m along the 6 km long, 3-C line. Along the refraction line, 10-kg charges were placed 1000 m apart for the first 5 km beginning from the east, 1320 m interval to the next one, and 1980 m intervals for the final four with a 1980 m gap to the beginning of the 3-C line.

The deployment of the Orion seismometers consisted of first choosing a suitable site that was a few metres off the seismic line and not directly adjacent to a shot hole. Next, the site was cleared of snow, levelled, and a patio stone was frozen in place. The

seismometer was then set up with the batteries, tested, and covered. The seismic crew was made aware of the positions of the Orion seismometers and their sensitive nature in an attempt to reduce truck-induced noise when the shoot was in progress.

To achieve sufficient velocity and depth resolution, the timing of the seismic shots must be precisely known relative to the seismic energy arrivals at the autonomous Orion receivers. For example, to achieve a depth resolution of 30 m in a unit of velocity 3000 m/s, a shot time precision of = 0.01 seconds (10 ms) is required. To achieve temporal precision of 1 ms with an accuracy of ±7 ms during the seismic shoot, a special GPS clock was interfaced with the operator's shot trigger inside the recording truck. The shot trigger would provide a +5 V pulse to trigger the external GPS box, which would then send a corresponding shot time stamp to be recorded by a terminal program running on a PC laptop. The GPS clock updated the PC clock every 60 seconds to correct for the slight drift from the absolute time occurring during this interval. As a consequence of this clock updating, every 60 seconds several seconds of dead time occurred during which a time could not be read. The operator needed to be aware of this to avoid triggering shots during the dead time interval. In addition, the drift had to be corrected during data reduction to guarantee the accuracy of the shot time recording because it could range up to 7 ms. Finally, the Nanometrics data management software provided with the seismometers, can only retrieve records precise to 1 second. This problem was easily solved during data reduction by applying a timing correction to the time of Orion seismic data, equal to the non-integral portion of the shot time recorded in the recording truck.

The acquisition procedure during the commercial shoot consisted of the shooters moving into position, turning off their trucks (if they were near an Orion station), hooking up the charge, and giving a signal to the operator. The operator would then check the status of the line, check the GPS clock, and fire the charge.

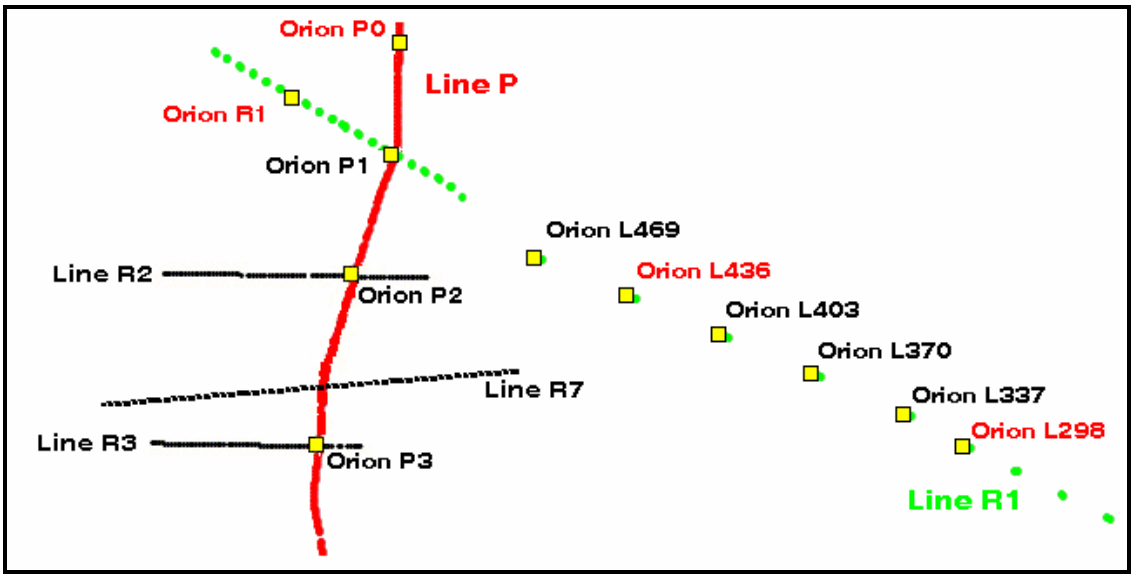

FIG. 3. Acquisition locations for data used in the modeling. Line P in red, Line R1 in green. Lines R2, R3, and R7 in black. The Orion seismometers with useable data are labelled in black. A red label instead indicates that data for that Orion could not be used due to GPS clock failures.

Data Reduction Technique

Data acquired by the Orion seismometers were stored in ring buffer files (private Nanometrics format). To reduce the data contained in each file, the following procedure was used with the Nanometrics Playback software: remove the unused portion of the ring buffer; extract the shot record from ring buffer into a compressed Nanometrics file; decompress the file; dump the decompressed data into an ASCII file; finally reformat the ASCII file for use in Matlab.

Most of the Orion seismometers were active during the shooting of several hundred shots among a total of ~1350 (12 seismic lines). To quickly carry on with the data reduction with the above procedure, a number of PERL programs were written to automatically compare files containing the times in which each Orion seismometer was active against a file listing all the shot times for all seismic lines. As a result of each comparison returning a positive match, the program wrote a command line in a batch file aimed at automatic execution of Nanometrics Playback reduction programs.

When run, the final batch operated the extraction, decompression, and dumping of each shot recorded by each Orion seismometer to an individual output ASCII file. Additional scripts were then used to reformat the ASCII data files for use in Matlab. A separate program created 12 ASCII files for every Orion, each file containing a list of all shot records from one seismic line only. The lists were used to read in data and create Orion receiver gathers in Matlab.

Because data were organized in receiver gathers, the first processing step in Matlab was to normalize shot records. A script was written to normalize all samples in each shot record by assigning the maximum amplitude a value of 1. A second script was written to use the CREWES program STAT (Margrave 1991) to shift backwards in time each shot record based on an input list of the non-integral portion of the shot times.

Data quality

Figure 4 displays a receiver gather of the 3C portion of radial line R1– vertical component – recorded by the Orion seismometer at the location closer to the intersection with Line P. As expected, the quality and appearance of data for the Orion compare to that of the traditional seismic shot gather for this same line (e.g. Figure 2 in Stewart et al. 2000).

Data from some of the Orion seismometers (labelled in red in Figure 3) could not be used, due to GPS clock failures.

Depth and tomographic models

After preliminary processing in Matlab, data were exported to Promax to exploit its processing capabilities. Pre-processing was completed with input and geometry definition. Some of the Orions (labelled in red in Figure 3) could not be used due to GPS clock failure. Line P had three Orion seismometers with good data, and Line R1 had five. Processing was completed with low pass filtering and Automatic Gain Control to improve the amplitude and continuity of the first breaks. Then first breaks were picked and exported to GLI3D to create a geologic model.

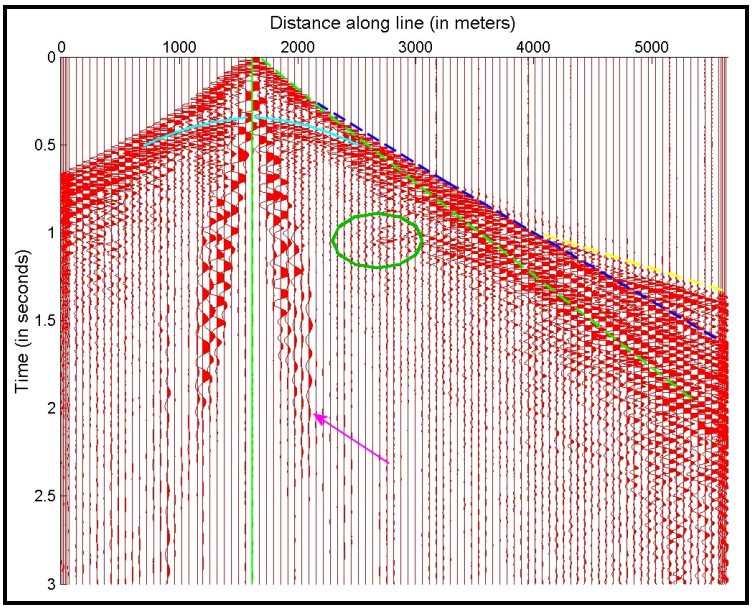

FIG. 4. Receiver gather for the 3-C part of radial line R1.The green line indicates the position of Orion 1. The magenta arrow indicates the ground roll; the green ellipse backscattered energy. The dashed green line indicates the direct arrival; the dashed blue and yellow lines indicate refracted energy, the latter a long offset refraction. Example reflected energy is indicated by the cyan hyperbola. The gather is very similar to a conventional reflection seismic gather (compare to Figure 2 in Stewart et al. 2000).

GLI3D uses ray-tracing through a defined initial depth model defined by the user. This is done by building velocity-depth information at selected control points within the survey (GLI3D Help Manual). At each control point an initial velocity estimate is made by finding a best fit to the First Breaks in GLI3D Offset Window. Additional velocity, thickness, or intercept time information can also be input in tables in the Set Control Point window. The initial model results are then inverted and a depth model created with GLI inversion (Generalized Linear Inversion).

A critical parameter to chose in building an initial model is the number of layers. Based on density logs, a 3-layer density model had been proposed (Excel Geophysics, 1996) as representative for most of the crater, other than the central uplift. In that model, Cretaceous shales form the top layer, with Devonian Carbonates and shales below the unconformity, and then a lower section of Devonian Carbonates and Anhydrites overlying the Precambrian basement. Density increases respectively from 2200 kg/m^3 to 2600 kg/m^3 to 2800 kg/m^3, for the three layers.

Based on similar examination of the sonic logs, a 3-layer velocity model seemed to us the most appropriate. To test the hypothesis, we initially attempted a 4-layer model, with two layers in the shallow section instead of just one, but we eventually abandoned it because the boundary between the first two layers was too poorly constrained, with a velocity change of only ~300 m/s.

Other important modelling parameters are the length of depth smoother and the length of velocity smoother. Because GLI3D uses ray tracing to create the final model, depth

smoothing is necessary to provide stability. A stable model is defined as that in which the values of the depth and velocity functions can be determined anywhere within the model (GLI3D Theory Manual).

For Line R1, a number of lengths were tried for the depth smoothing: lengths <2500 seemed to cause a failure of the program to ray trace travel times; for lengths >4500 no major difference was noticed in the final depth and velocity models for this line, nor further minimization of the residual errors. A length equal to $1/5^{th}$ of the longest source-receiver offset is suggested as a good trade-off between stability of the final model and resolution (GLI3D Help Manual). The longest source/receiver offset is ~17.5 km, and therefore a depth smoother of 3500 m was finally chosen. A much longer velocity smoother than the depth smoother is recommended: it seems that GLI3D works best when it forces all rapid variations to take place in the thickness and not the velocity (GLI3D Help Manual). A number of lengths were tried, and a length of 12000 m provided the model with lower residual errors when combined with a depth smoother of 3500. For consistency, the same smoothing lengths were used for Line P.

To further improve stability of the final model, the first model was constrained by entering thickness information in the Set Control Point window, based on available well logs (for instance well 1 and well 2, which are very close to Orion P1 and Orion L469, respectively). Then intercept times, velocity, and thicknesses were modified at all control points until a model was found that best tied with the wells at the control points and all other wells. Due to the small number of Orions the model is under constrained, and this procedure assured the greatest confidence possible in the final modelled depths and velocities. Particular care was taken to honour field data, especially for Orion P1 at the intersection of the two lines, the location where the velocity models were to be compared. Comparison of Figure 5 and Figure 6 demonstrates how the described procedure has been instrumental in building a satisfactory model. It also illustrates the non uniqueness of the GLI3D solution. The two initial models were built with identical smoothing options, and the same initial thickness and velocity estimate in the Offset Window. Once the velocity logs for well 3 and well 4 were considered, some minor adjustments were made to the initial model. The adjustments resulted in a substantially different velocity model for layer two, in spite of very similar depth models and residual errors. As described in more detail in the next section, the model in Figure 6 has a overall better tie with the available wells.

Once the first model was defined, the model was inverted. GLI3D only allows shot gathers with shots as control points. With very few receivers and a large number of sources this was a problem, and the inverted models were rather unstable, in spite of the additional constrains used. The reason is that each control point only had 5 receivers for Line R1, and only 3 for Line P. That means there were only a few ray traced travel times to compare to the observed travel times. All models created with this geometry were unstable, in that they had very large residual errors.

To be able to use receivers as control points and to undertake modelling more efficiently, we went back to Promax and redefined the survey geometry, treating each receiver as a source and vice-versa. The resulting pseudo-receiver first break gathers were exported to GLI3D and allowed modelling with better minimization of residual

errors. This procedure also guaranteed greater control in the vicinity of the receivers, a critical factor considering that the scope of the study was to compare velocities at the receiver location at the intersection of the two lines (Orion seismometer P1).

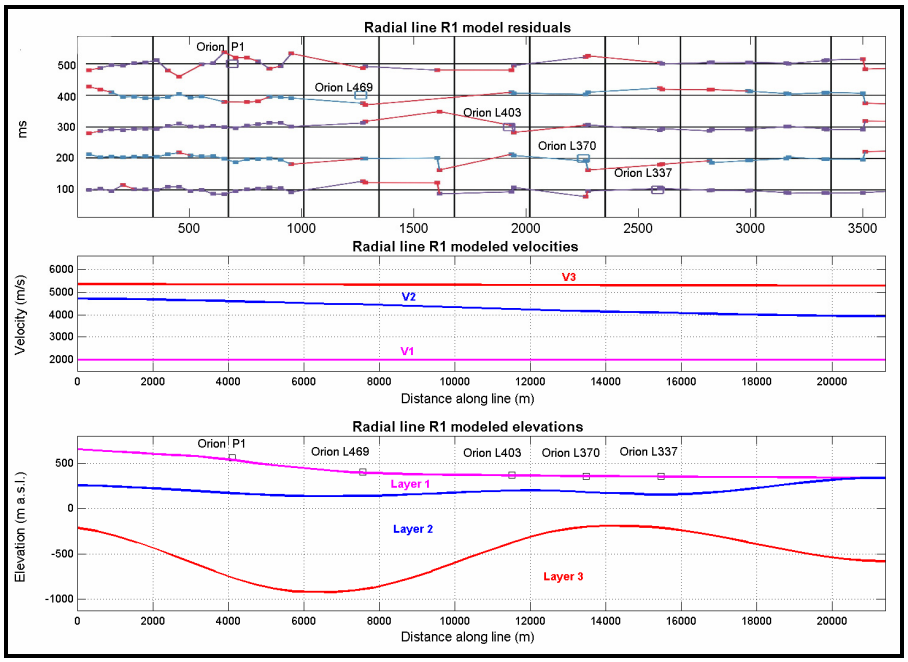

FIG. 5. Depth (bottom display) and velocity (middle) models for radial line R1 produced with GLI3D, with residual error (top display). The top display shows residual errors for each Orion seismometer. Compare to Figure 6.

The depth model in GLI3D has elevation and velocity represented by continuous, smoothed polynomial functions in x and y (internal GLI3D processing coordinates system based on survey coordinates). The model that is finally exported to Matlab is a gridded model that GLI3D derives from the depth model, with depth and velocity values defined at discrete, regularly spaced locations. The grid size provides a measurement of the resolution of the final model. For this study the resolution was of 610 m for Line R1 and 545 m for Line P. Tomographic models were also created with the TOMO inversion, using the inverted depth model as an initial model. Both depth and tomographic models were exported to Matlab as ASCII files. In Matlab, a number of plots were created to compare the resulting models with previously published ones (i.e. Mazur et al., 2002), and to investigate velocity anisotropy.

Discussion

The final 3-layer model for Line R1 is plotted in Figure 6. The bottom display shows the depth model. The middle display shows the velocity model. Notice that in this model, velocities can vary laterally within each layer but not vertically (as opposed to the tomographic model). The top display in Figure 6 shows the residual errors in ms.

GLI3D calculates the error as RMS deviation between the actual first breaks and the modelled first breaks (GLI3D Help Manual) at each receiver, for each shot.

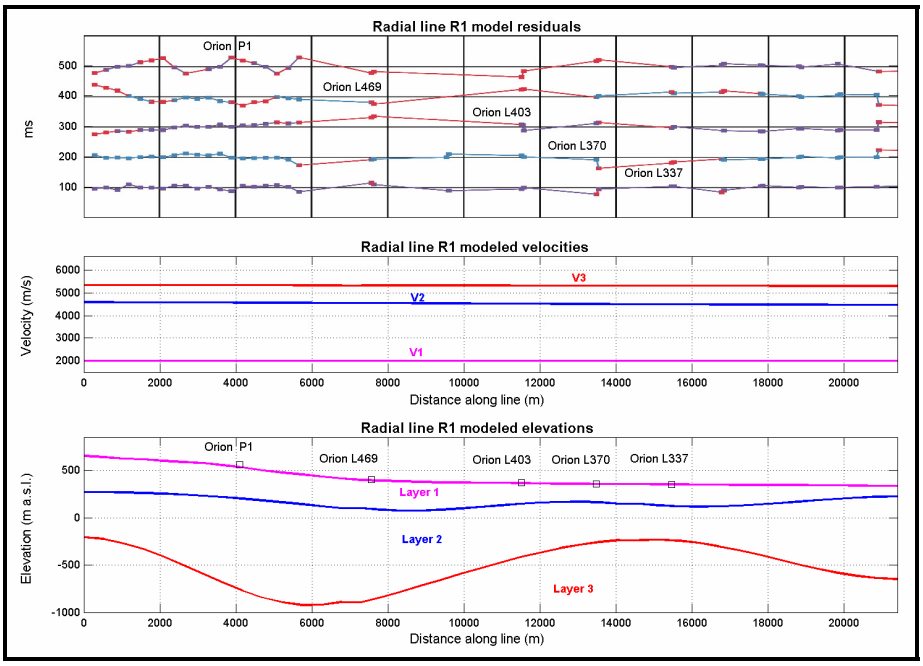

FIG. 6. Depth (bottom display) and velocity (middle) models for radial line R1 produced with GLI3D. The top display shows residual errors for each Orion seismometer.

It is interesting to note that for each Orion there seems to be a symmetric structure in the errors at the seismometer location. The effect is most acute for Orion P1 because of the greater number of shots at short offsets and consequently a greater sensitivity to velocity changes in the shallow depths. The error is positive at the Orion location, then negative at distances greater than ~500 m on either side of the Orion, then positive again at distances greater than ~1500 m on either side of the Orion, meaning that the modelled travel times are shorter, then longer, then again shorter than the observed travel times respectively. This suggests a varying velocity for layer one, as opposed to the constant velocity of 2000 m/s used in the model.

As it was expected, the modelled depth structure is very similar to that proposed by Mazur (2000) and Mazur et al. (2002), with the exception of the number of layers for the shallow section.

In Figure 7, bottom display, the depth model is compared to 3-layer velocity logs at well locations. Above-sea-level depths are used so as to study the structure independent of topography. The top of Layer 2 is compared to the unconformity, and the top of Layer 3 to the top of the Slave Point. The choice of a 3-layer velocity model was based on the aforementioned review of density studies and examination of the available sonic logs, as well as GLI3D modelling constraints. We consider the associated depth model fairly accurate representation of velocity layering across the crater. It is important to observe, however, that the lateral variation in geology across this section is high, as we move from rim uplift (well 1) to the area of slumped fault blocks, to the central uplift (well 3) and then to the area of slumped fault blocks on the eastern side of the uplift. The complexity of the geology of the crater is illustrated in the West-East cross section in Figure 8 (after Hildebrand et al. 2001).

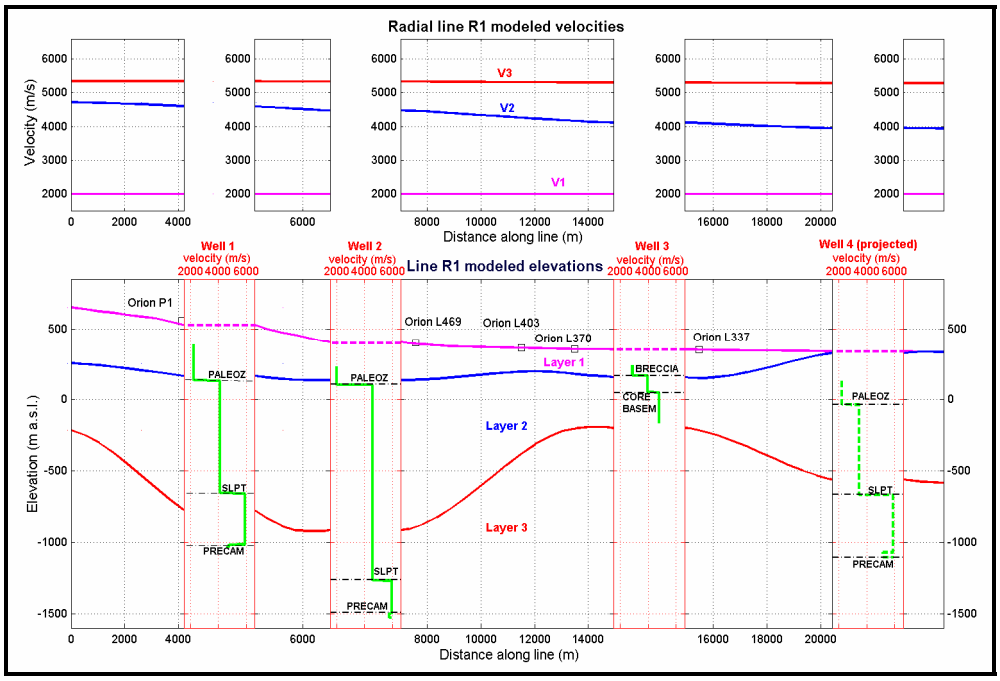

FIG. 7. Radial line R1 modelled depths and velocities produced by GLI3D are compared to blocked three-layer velocity logs from all available wells.

For the unconformity, there seems to be a good agreement between the model and the well tops especially at wells 1 and 2. The model plotted in Figure 5 showed a better agreement between the top of layer 2 and the unconformity at each of the four wells; the model in Figure 6 showed a poorer tie between the top of layer 2 and the unconformity at well 4, but was preferred because of the better tie between the model velocity for layer 2 and the well log velocities at all four wells.

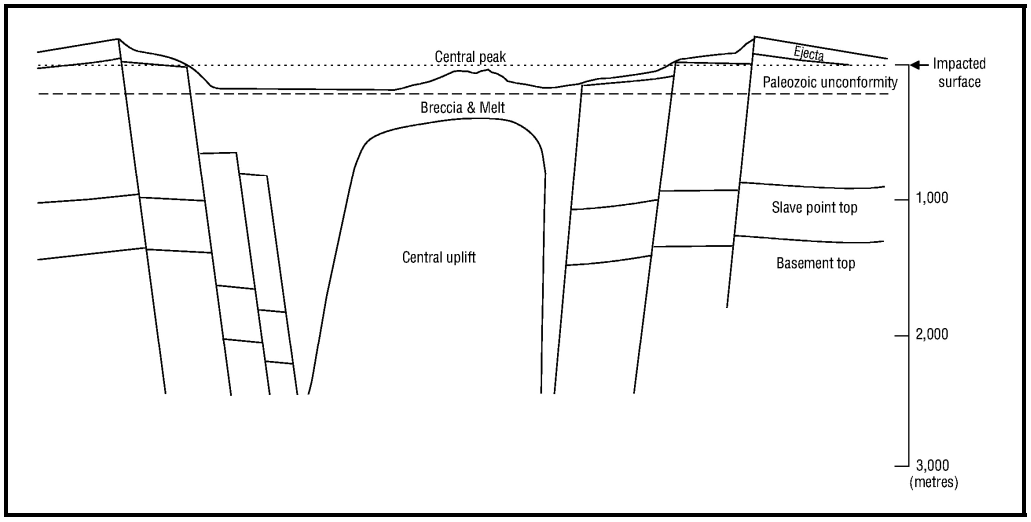

FIG. 8. Schematic structural cross section of the Steen River crater (after Hildebrand et al. 2001). The dotted line shows the projected location of the impacted surface; the dashed line shows the approximate level of erosion that had occurred before the transgression of the Cretaceous sea buried the crater. The crater's three main structural elements are the zone of slumping, collapsed disruption cavity filling, and central structural uplift.

To achieve depth tie at well 4, was considered less important than the overall velocity tie in consideration that well 4 was projected more than 1000 m from the zone of slumped, deformed blocks outside the disruption cavity, with no seismic line to assist the projection. Notice also the corresponding lack of modeling constraints east of Orion L337, due to the failure of Orion L298.

As for the depth location of the velocity jump associated with the top of the Slave Point, there is a good agreement between the model and well 1. The tie is not as good with well 2 and well 3. While the model still provides a realistic representation of the structure of the crater, the central uplift is limited to ~700 m as opposed to the ~1100 m indicated by the wells. One possible explanation for this result is that the model is smoothed. As previously mentioned the model is under constrained for both lines. For Line R1, GPS clock failures reduced the receivers with reliable data to 5, out of the 8 deployed. For these reason a long depth smoothing to minimize residual errors and obtain a stable model was necessary.

The well log velocity for the unconformity increases from ~4130 m/s (at well 1) to ~4590 m/s (at well 2), then decreases to ~3970 m/s (at well 3), and finally to ~ 3460 (at well 4). These velocities can be compared against the modelled velocity plotted in the top displays in Figure 7. The modelled velocity (V_2) is very smooth but shows a tendency to decrease eastward, from ~4595 m/s (at well 1 location), to ~4470 m/s (at well 2 location), to ~4120 m/s (at well 3 location) to ~3450 m/s (at well 4 location). A possible explanation for some of these differences (i.e. where the refraction velocity is higher than the well log velocity) is that the ejecta lying on the Palaeozoic slumped blocks may contain in places blocks of faster Precambrian rocks as a result of the impact. In that case the refracted energy would travel at an higher average velocity than that measured by the well logs. Also, the described log values represent a velocity averaged over several hundred meters.

The well log velocity for Layer 3 initially increases slightly from ~5935 m/s (well 1) to ~5985 m/s (well 2) then decreases to ~4770 m/s (well 3) and finally goes up again to ~ 5870 m/s (well 4). These velocities are recording very different geology in the structural elements of the crater. Well 3 had apparently penetrated the central uplift immediately below the unconformity, encountering ~120 m of clay altered vesicular rocks directly above the basement rocks (Hladiuk et al., 1999). These vesicular rocks explain the low velocity at this location.

In contrast, the modelled velocity (V_3) is again very smooth showing only a slight decrease eastward, from 5335 m/s (at well 1 location) to ~5300 m/s (at well 4 location). This velocity is overall lower than that from the well logs described above, with the exception of well 3. A possible explanation for this may be fracturing of the Lower Devonian and Precambrian formations inside the crater rim (concentric fracturing, i.e. fracturing with strike orthogonal to the direction of propagation of the seismic waves for Line R1). Refracted waves travel a great distance and their velocity is affected by both the small scale and large scale heterogeneity of the rocks. On the contrary, the depth of investigation of the sonic log is only a few centimetres. Therefore, while this measurement can record the small scale heterogeneity of the rocks, it is very unlikely to record large scale, fracture induced velocity changes. In addition, the well logs are a

measure of vertical velocity whereas the refraction velocities are horizontal velocities. A lower horizontal velocity than vertical velocity is confirmed experimentally in the case of dry vertical fractures (Thomsen 1994).

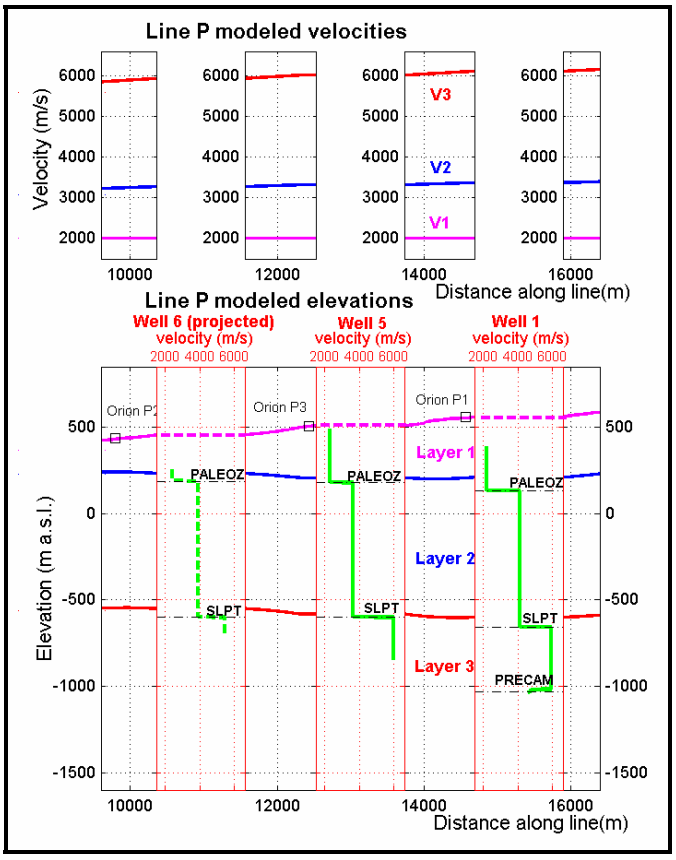

FIG. 9. Parallel line P modelled depth and velocities produced by GLI3D are compared to blocked three-layer velocity logs from all available wells.

For Line P, a stable velocity model was only obtained when limiting the maximum offset used in the inversion to ~ 6500 m. The model is plotted in Figure 9 with residual errors in the top display. For part of the model, errors are still as high as ~50 ms, especially for Orion P3, but they are low for all three seismometers for the area between Orion P2 and Orion P1. In addition, the model ties well with the 3 available wells, as shown in Figure 9. This gives confidence in the modelled velocities and allows comparison with the velocity model for Line R1.

The depth and velocity models for Line P and Line R1 are compared at well 1 in Figure 10. Figure 11 shows the tomographic models compared at the well tie, with superimposed layer model. The good fit between the two models, and with the well, gives some confidence in the velocities at this particular location. In Figure 10, Layer 1 velocity is 2000 m/s, constant for Line P and Line R1. This was a modelling assumption, supported by well log information. Layer 2 velocity at the well tie is ~3370 m/s for Line P and ~4595 m/s for Line R1. A difference of ~ 27% cannot be explained in terms of fracturing alone. In facts, most rocks are considered weakly anisotropic, and rarely exceed 20% anisotropy (Thomsen 1986).

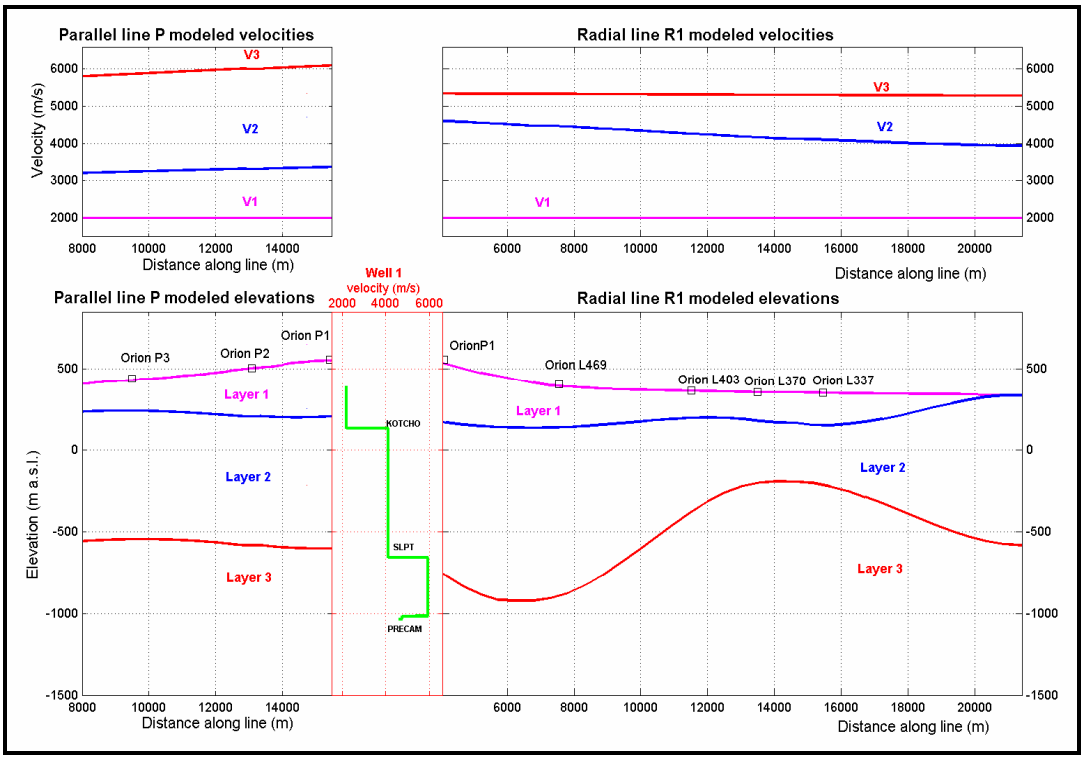

FIG. 10. Modelled depths (bottom display) and velocities (top display) for parallel line P and radial line R1 are compared at Well 1. Notice the good depth tie and the significant velocity anisotropy at the well location.

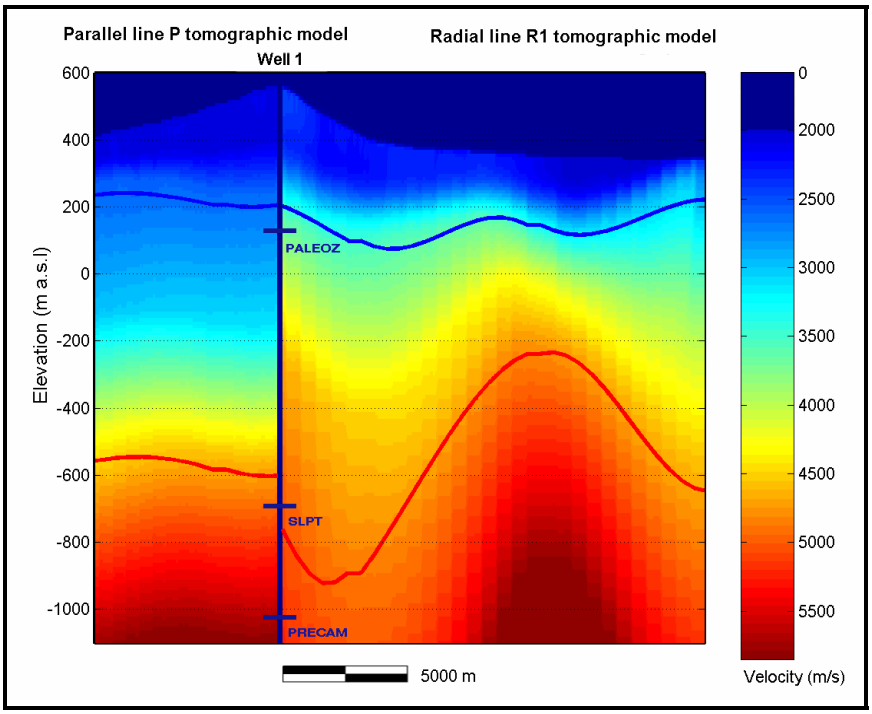

FIG. 11. Tomographic models for parallel line P and radial line R1 compared at well tie. Depth model is superimposed for reference. Notice the good depth tie and the significant velocity anisotropy at the well location.

As hypothesized earlier, the ejecta layer overlying the slumped blocks formations below the unconformity probably contain blocks of Precambrian rocks between the crater's rim and the central uplift. This would affect the velocity of Layer 2 for Line R1, shot across the crater's rim and core, but not for Line P, shot parallel to the rim. This effect may or may not be combined with anisotropy due to radial fracturing. Layer 3 has a higher velocity (~6100 m/s) for Line P than for Line R1 (~5350). A difference of ~13% may be explained in terms of fracturing alone, with concentric fracturing of the Lower Devonian (Slave Point) and Precambrian at the crater rim.

This, however, would imply two different fracturing systems, one radial for the formations immediately below the unconformity if the velocity difference described in the paragraph above is due to preferential fracturing, and one concentric for the Lower Devonian and Precambrian formations. Although this is certainly possible in some geological situations, it is unlikely in the case of impact generated fracturing. Further studies are required to provide a definitive explanation.

WORK CURRENTLY IN PROGRESS

3-D depth models

A 3D model has been created for Line P. Line R1 runs straight from the crater's centre to the rim. We have sufficient confidence in the structural symmetry of the crater and therefore in the validity of a 2-D model for this line. On the other hand line P is crooked and has faster formations at shallower depths on the outside of the crater, making a 3D model necessary to explore the possible influence of out-of-plane refractions on the velocity models: having constrained the depths to top of Layer 2 and top of Layer 3 using depths from vertical wells along the line would force lower velocities in the case of out of plane refractions.

The 2-D model for line P and a 2-D section extracted from the 3-D model are compared in Figure 12. The bottom displays show a portion of the reflection line P with superimposed GLI models, 2-D in a and 3-D in b, respectively.

These models, originally in depth have been converted to a pseudo-time model to allow the comparison; in both the 2-D case and 3-D case, a constant velocity of 3500 m/s was used to convert to two-way travel layer 2 thickness.

Although a preliminary result, model inspection offers useful insights. Both the 2-D and 3-D algorithms have modelled with sufficient accuracy the Cretaceous unconformity. As for the Slave Point, the 2-D algorithm, although constrained using the depths to the Slave Point from the three wells, has failed to model the topography of the top of the formation. The 3-D algorithm, on the other hand, has been successful in modeling the anticline in the Slave Point top below Orion P2. Below Orion P3, the 3-D algorithm seems to have produced a poorer result. This however must be considered in light of the constant coefficient used to convert the depth model into a pseudo-time model. Indeed, the velocity for Layer 2 decreases significantly in the 3-D model. A conversion velocity of 3150 m/s would pull up the Slave Point at the correct time below Orion P3. A more robust depth to time conversion is being performed based on the model velocity and velocity logs from wells.

The top displays in Figure 12 show the modelled velocities. Layer 2 and Layer 3 velocities have slightly lower values in the 3D model at both Orion P2 and Orion P3 locations. The velocities are very similar in the two models at the Orion P1 location, where line P intersects line R1. This result confirms the presence of velocity anisotropies at the Orion P1 location, where the two orthogonal lines intersect, although further studies will be necessary to provide a conclusive interpretation and better separate structural from fracture induced velocity anisotropies.

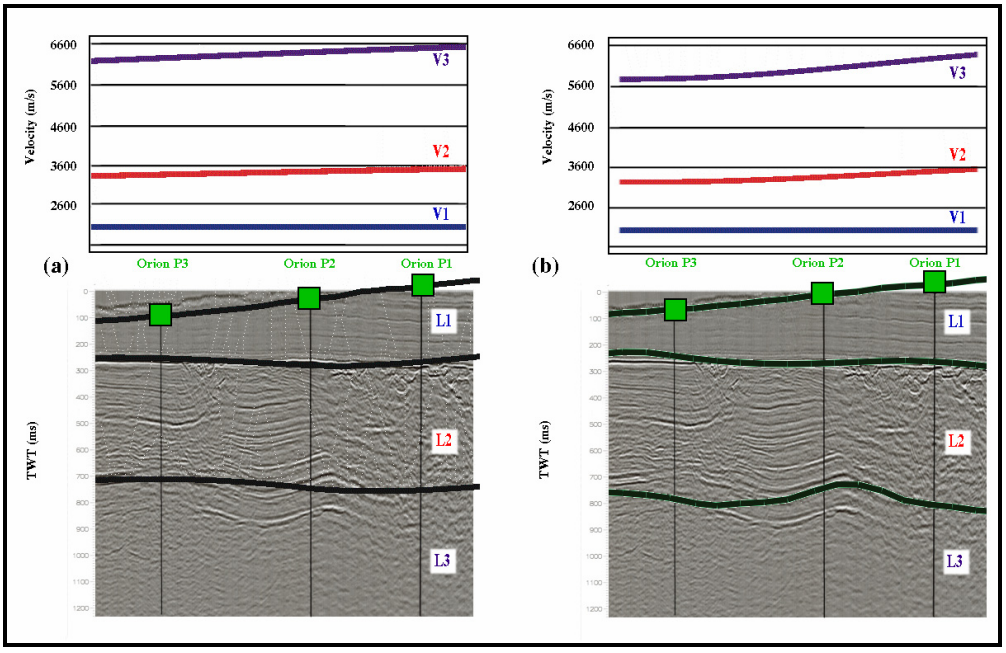

FIG. 12: Comparison of a 2-D model (a) and a 2-D section from a 3-D model (b) generated in GLI3D for parallel line P. Modelled velocities are in the top displays. In the bottom displays the depth models are shown converted to pseudo two-way travel time and superimposed to the time migrated reflection line (courtesy of Penn West Petroleum). V indicates velocity, L indicates layer. The 2-D algorithm, although constrained using the depths to the Slave Point from the three wells, has failed to model the topography of the top of the formation. The 3D algorithm has well modelled the anticline below Orion P2, but failed to model the anticline below Orion P3.

Interval velocity determination

Study of reflection interval velocities can assist in the interpretation of the observed anisotropy effects and it is currently under way. The velocity analysis has been carried out on line P and radial line R7, both of which provided by Penn West Petroleum Ltd.

Because of the complex nature of the Steen river structure, DMO correction has been included in the processing flow to make the velocity analysis dip independent. The processing has been carried out at Geo-X Systems Ltd., with the flow described in Figure 13 (after Yilmaz 2001).

Steps 5 to 7 in the processing flow have been implemented in Geo-X's proprietary VVS module (Variable Velocity Stacks). VVS allows simultaneous analysis of CMP gathers and direct stack response to the picked velocity. Examples of velocity analysis with the VVS are shown in Figure 14 and Figure 15, for parallel Line P1 and radial line

R7, respectively. In both figures, the first panel on the right shows the RMS velocity function and the interval velocities; the second panel is the semblance plot; the third panel is the offset gather, and the last panel on the left is the real time DMO stack. Velocities were picked using a combination of maximum energy on the semblance plot (red arrow) and maximum focus of the reflector in the stack display (red rectangle).

1. Velocity analysis
2. NMO correction at sparse locations using flat-event velocities
3. DMO correction
4. Inverse NMO correction with velocities used in step 2
5. Velocity analysis
6. NMO correction with updated velocities
7. Stacking

FIG. 13. DMO velocity analysis processing flow (Yilmaz 2001).

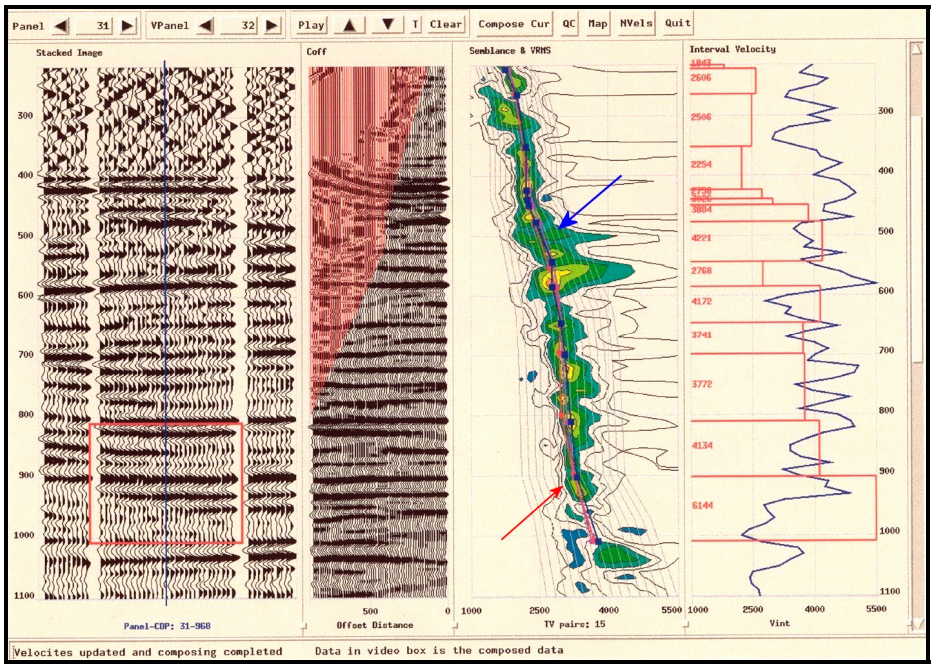

FIG. 14. Variable velocity stack display for line P. From right to left: velocity display (RMS function in blue, interval velocities in red), semblance plot, offset gather plot, DMO stack display. The red arrow in the semblance plot and red rectangle in the DMO stack display indicate the current pick. The blue arrow in the semblance plot points at the Cretaceous unconformity; compare to Figure 15.

The simultaneous use of a Quality Control display with overlay of time picks, interval velocity field, and final stack, allowed construction of a structure consistent interval velocity model. An example of the QC display is shown in Figure 16 for the portion of line R7 outside the crater's rim. The time of the picks can be changed in this display and

the velocity field and final stack are updated accordingly. The modelling was constrained using velocities and times from velocity logs converted to two-way travel time, as well as the final time migrated seismic sections provided by Penn West.

A preliminary consideration about anisotropy effects can be made by looking at the semblance plots and interval velocity displays in Figures 14 and 15. The blue arrows in the figures indicate the location of the Cretaceous unconformity.

This preliminary result, confirms the hypothesis that radial fracturing exists for the formations immediately below the unconformity, combined with some structural effects. The final interval velocity models are being completed and will be superimposed to the final time migrated seismic sections, to allow a complete and simultaneous investigation of the interval velocities and the geologic structure from the seismic lines and possibly separate structural induced from fracture induced anisotropy. The corresponding interval velocities are significantly different: ~4220 m/s for the parallel line and ~ 5750 for the radial line, again a 27% difference.

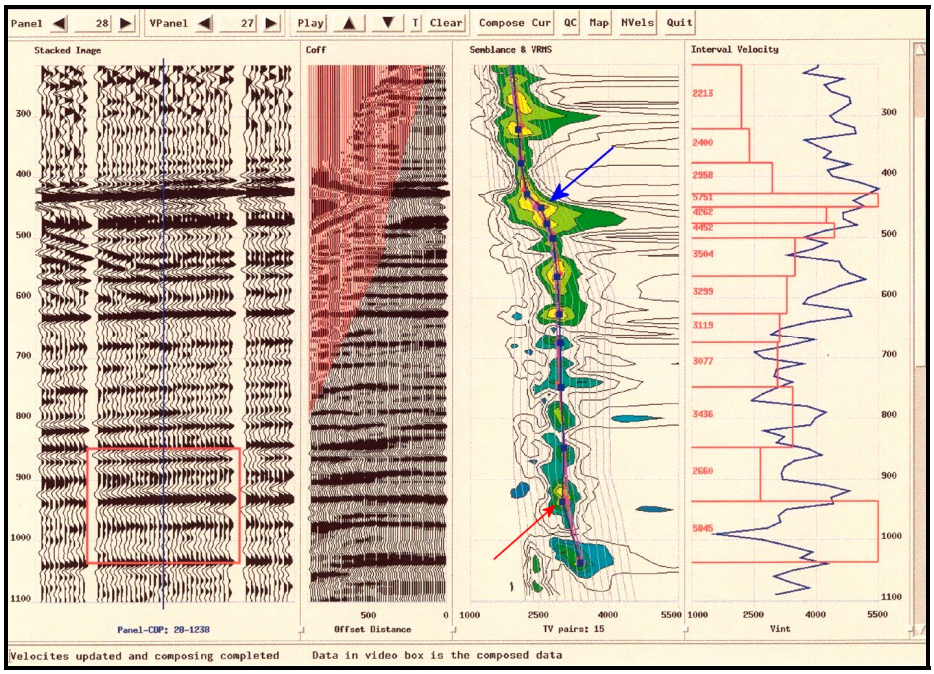

FIG. 15. Variable velocity stack display for line R7. From right to left: velocity display (RMS function in blue, interval velocities in red), semblance plot, offset gather plot, DMO stack display. The red arrow in the semblance plot and red rectangle in the DMO stack display indicate the current pick. The blue arrow in the semblance plot points at the Cretaceous unconformity.

ACKNOWLEDGEMENTS

We wish to thank Mike Mazur for the field deployment and data acquisition by the Orions, and Don Hladiuk, Armin Shafer, and Ray Prudholme of the then Gulf Canada Resources for survey support; we also thank the seismic survey crew from Fastway Exploration and the operator, Ron Bell; the 3-component seismometers were supplied by the Geological Survey of Canada, Natural Resources Canada, and David Eaton of the University of Western Ontario; the shot recording/timing device was loaned by GSC

Ottawa. We thank David Brydon, Henry Bland, and Claudio Costi for the precious discussions about the logic of Perl and support during the programming; Kevin Hall and John Millar for support during Matlab programming; we also thank Belinda Jensen and Leo Macht at Geo-X for DMO processing and technical support during velocity analysis; we thank Rob Stewart for the useful discussion on 3D refraction modeling; finally, we thank Erwin Unger at Penn West, for his support and the useful talks on seismic interpretation of the Steen River structure, and Anne Thompson, who graciously authorized use of the seismic data for the interval velocity analysis.

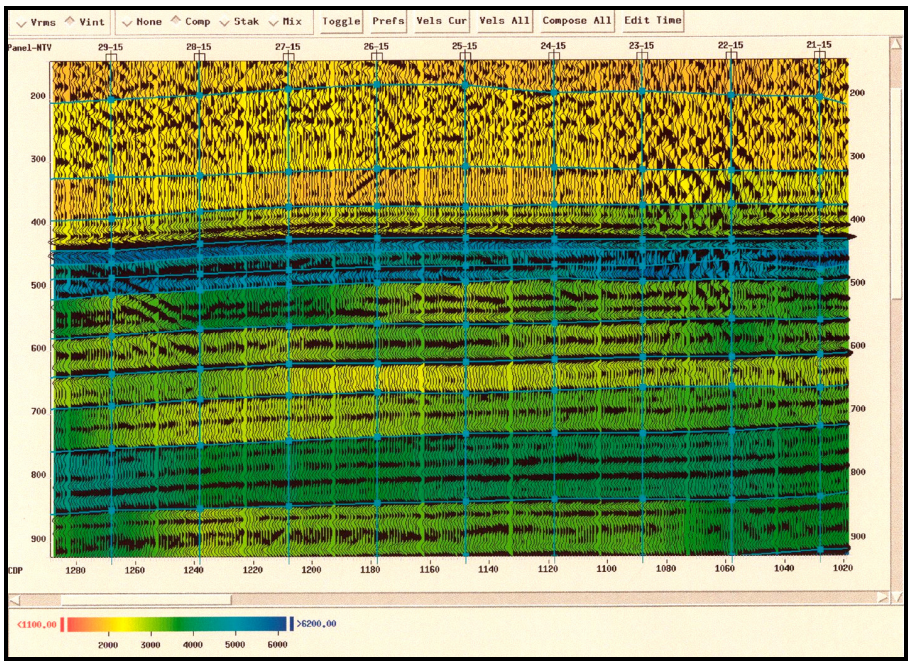

FIG. 16. Quality Control display with time picks, final stack, and interval velocity overlay. The time of the picks can be changed in this display and the velocity field and final stack are updated accordingly.

REFERENCES

Bates, C. R., Lynn, H. B., and Simon, M., 1999, The study of a naturally fractured gas reservoir using seismic techniques: American Association of Petroleum Geologists Bulletin, **83**, 1392-1407.

Carrigy, M. A., and Short, N. M., 1968, Evidence of Shock metamorphism in rocks from the Steen River Structure, Alberta: in French, B. M. and Short, N. M., (eds.), Shock Metamorphism of Natural Materials, Mono Book Corp., Baltimore, MD, 367-378.

Fritz, R.J., W.H., Cecile, M. P., Norford, B. S., Morrow, D., and Geldsetzer, H. H. J., 1991, Cambrian to Middle Devonian assemblages: in Geological Society of America, The Geology of North America, v. G-2.

Hampson-Russell Software Services Ltd., 2002, GLI3D Help Manual.

Hildebrand, A. R., Mazur, M. J., Schafer, A., Hladiuk, D. W., Stewart, R. R, and Pilkington, M., 2001, Seismic velocity imaging of the Steen River Crater: technique development for exploring crater reservoirs: 2001 Final Report for Research Project Agreement No. 1365.

Hildebrand, A. R., Mazur, M. J., Stewart, R. R., Hladiuk, D. W., Schafer, A., Schoenthaler, L., Pilkington, M., 2000, Structure and hydrocarbon occurrences of the Steen River Astrobleme: GeoCanada 2000 abstracts, CD format.

Hildebrand, A. R., Pilkington, M., Grieve, R. A. F., Stewart, R. R., Mazur, M. J., Hladiuk, D. W., and Sinnott, D., 1998, Hydrocarbon potential of the Steen River impact structure, Alberta, Canada: Am. Ass. Pet. Geol. 1998 Annual Convention Abstracts, CD format.

Hladiuk, D.W., Schafer, A., Schoenthaler, L., Hildebrand, A.R., Stewart, R.R., Mazur, M., Pilkington, M., Grieve, R.A.F., and Sinnot, D., 1999, Hydrocarbon potential of the Steen River impact structure, Alberta, Canada: Can. Soc. Pet. Geol. 1999 Annual Convention Abstracts, CD format.

Innes, M. J. S., Pearson, W. J., and Geuer, J. W., 1964, The Deep Bay crater: Publications of the Dominion Observatory, **31**, 19-52.

Lynn, H. B., Simon, K. M., and Bates, C. R., 1996, Correlation between P-wave AVOA and S-wave traveltime anisotropy in a naturally fractured gas reservoir: The Leading Edge, **15**, 931-935.

Mazur, M. J., Hildebrand, A. R., Hladiuk, D. , Schafer, A., Pilkington, M., Stewart, R.R., 2002: The Steen River Crater Seismic Refraction Project. In Lunar and Planetary Science XXXIII, Abstract # 1736, Lunar and Planetary Institute, Houston (CD-ROM).

Mazur, M. J., 2000, Seismic Velocity Imaging of the Steen River Crater: Technique Development for Exploring Crater Reservoirs: Industry report.

Melosh, H. J., 1989, Impact Cratering: A Geologic Process, Oxford Monographs on Geology and Geophysics No. 11, Oxford University Press, 245 p.

Niccoli, M., and Hildebrand, A., 2003, Understanding Impact-Generated Hydrocarbon Reservoirs: May 2003 Research report, for Research Project Agreement No. 1478.

Robertson, G. A., 1997, The Steen River Structure, Alberta, Canada: Subsurface Identification and Hydrocarbon Occurrences, in Johnson, K.S., and Campbell, J.A. (eds.), Ames structure in north-western Oklahoma and similar features: origin and petroleum production (1995 symposium): Oklahoma Geological Survey Circular 100, 385-390.

Sawatzky, H. B., 1976, Viewfield – a producing fossil crater. J. Can. Soc. Expl. Geophys., **8**, 22-40.

Excel Geophysics Inc., 1996, Steen River Gravity Interpretation, Industry report.

Tsvankin, I. and Lynn, H.B., 1999, Special section on azimuthal dependence of P-wave seismic signatures - Introduction: Geophysics, **64**, 1139-1142.

Thomsen, L., 1986, Weakly elastic anisotropy: Geophysics, **51**, 1954-1966.

Winzer, S. R., 1972, The Steen River Astroblem, Alberta, Canada: 24th International Geological Congress, Planetology, Section 15, 148-156.